

# The positioning of stress fibers in contractile cells minimizes internal mechanical stress

Lukas Riedel<sup>a,b</sup>, Valentin Wössner<sup>c,d</sup>, Dominic Kempf<sup>a</sup>, Falko Ziebert<sup>c,d</sup>,  
Peter Bastian<sup>a \*</sup>, Ulrich S. Schwarz<sup>a,c,d \*</sup>

<sup>a</sup>Interdisciplinary Center for Scientific Computing, Heidelberg University, Heidelberg, Germany

<sup>b</sup>Institute for Environmental Decisions, ETH Zürich, Zürich, Switzerland

<sup>c</sup>Institute for Theoretical Physics, Heidelberg University, Heidelberg, Germany

<sup>d</sup>BioQuant, Heidelberg University, Heidelberg, Germany

October 15, 2024

## Abstract

The mechanics of animal cells is strongly determined by stress fibers, which are contractile filament bundles that form dynamically in response to extracellular cues. Stress fibers allow the cell to adapt its mechanics to environmental conditions and to protect it from structural damage. While the physical description of single stress fibers is well-developed, much less is known about their spatial distribution on the level of whole cells. Here, we combine a finite element method for one-dimensional fibers embedded in an elastic bulk medium with dynamical rules for stress fiber formation based on genetic algorithms. We postulate that their main goal is to achieve minimal mechanical stress in the bulk material with as few fibers as possible. The fiber positions and configurations resulting from this optimization task alone are in good agreement with those found in experiments where cells in 3D-scaffolds were mechanically strained at one attachment point. For optimized configurations, we find that stress fibers typically run through the cell in a diagonal fashion, similar to reinforcement strategies used for composite material.

---

\*Authors for correspondence: Peter Bastian (peter.bastian@iwr.uni-heidelberg.de) and Ulrich S. Schwarz (schwarz@thphys.uni-heidelberg.de)

# 1 Introduction

The mechanics of animal cells is determined mainly by the actin cytoskeleton, a highly dynamic network of semiflexible filaments that can form different architectures within the same cells [1, 2, 3]. For example, during cell migration rapidly polymerizing and branched actin networks are used to push the cell front forward, while contractile actomyosin networks and bundles are used to retract the rear of the cell [4]. Early work with light and electron microscopy of cultured cells discovered that in mechanically stressful situations, cells often form clearly visible actin filament bundles called stress fibers [5]. They are also formed *in vivo* when mechanical stress arises, e.g. during development, wound healing or in the vasculature [6]. In general, it is believed that their main function is adaptation to mechanically challenging conditions of the environment [7, 8, 9].

The detailed investigation of stress fibers has revealed that they have a large and diverse range of cellular functions, including cell shape control, mechanosensing and wound closure, and that they come in different flavors that differ in cellular location and composition [10, 11]. For example, dorsal stress fibers growing out of cell-matrix adhesions at the cell front have been shown to be composed mainly of actin and its crosslinker  $\alpha$ -actinin, while transverse arcs form perpendicular to it and in addition contain the molecular motor non-muscle myosin II, thus making them contractile [10]. The strongest stress fibers are the highly contractile ventral stress fibers that connect focal adhesions at the ventral side of a cell. They typically result from the fusion of dorsal stress fibers and transverse arcs [10, 12]. Peripheral or cortical stress fibers are also contracting between two anchoring focal adhesions and are responsible for the invaginated shapes of contractile cells adhering at discrete sites of adhesion, which form by a balance of bulk contractility in the cell and line contractility along the periphery [13, 14]. In contrast to ventral stress fibers, peripheral stress fibers are not formed by other stress fibers, but through a condensation process from the actomyosin cortex [15, 16]. Because they are contractile and directly connected to the extracellular environment, ventral and peripheral stress fibers also act as mechanosensitive organelles that inform the cells about the mechanical status of their environment [17]. Because stress fibers typically are formed when cells are cultured on relatively stiff substrates [18, 19], their mechanosensitivity must be such that large stresses promote their assembly, in agreement with the overall interpretation that they have a mechanoprotective function and form on demand in order to shield cells from excessive mechanical stress, although this never has been proven directly.

Besides filamentous actin, the two main molecular components of stress fibers are the actin crosslinker  $\alpha$ -actinin and the molecular motor non-muscle myosin II. Non-muscle myosin II in stress fibers is organized into 300 nm large minifilaments that alternate with regions held together by  $\alpha$ -actinin [20]. Because of this sarcomeric structure of transverse arcs as well as ventral and peripheral stress fibers, biophysical models for stress fibers often focused on their similarities and differences to muscle filaments [21]. The standard way to probe their mechanical properties is laser cutting, which typically leads to exponential relaxation curves

that can be used to estimate internal stress and motor activity [22, 23, 24]. Similar responses have been reported for stress fibers stretched and compressed on soft elastic substrates [25]. Stress fibers can also be dissected out of cells and their mechanical properties measured with micromanipulators [26, 27]. Together, these experiments show that stress fibers are well-defined, discrete organelles that have very different mechanics than the bulk of the cell.

Starting from their similarity with muscle fibers, mathematical models for stress fibers usually consider a linear array of contractile elements [28, 29, 30]. These sarcomeric units produce force according to the crossbridge cycle of the myosin II molecular motors. By taking the continuum limit of many sarcomeric units, a continuum theory for stress fibers can be formulated [31]. One-dimensional models for stress fibers can be solved numerically by standard methods such as finite differences or finite elements, but usually are not scaled up to whole-cell models due to computational challenges and the underlying molecular complexity. Recently, the immersed boundary method was used to study different rheological models for stress fibers embedded into a bulk material representing the cell [32], but no procedure has been developed before to predict where they will be positioned in mechanically challenged cells.

In order to study the effect of the actin cytoskeleton on the level of whole cells, often filament models are used in which individual polymers of a certain length are considered as one-dimensional beams, which can be bent and stretched. Additionally, these filaments might be subject to Brownian dynamics, leading to stochastic partial differential equations, which can numerically be studied e.g. with the finite element method (FEM) [33, 34]. The dynamics can then be scaled up to networks, like the actin cortex, consisting of crosslinked and/or contractile filaments. Depending on the amount of deformation, these networks transition from being entropy to bending and finally to being stretching dominated [34]. Cooperative effects between filaments give rise to nonaffine displacements [35] and strain hardening [34].

In order to include the muscle-like contraction of stress fibers and at the same time to achieve a whole-cell description, earlier work has used a continuum approach based on FEM, that predicted in which directions fibers form in adherent contractile cells [36, 37, 38]. Muscle-like contractile elements were connected to an anisotropic contractile material by specifying at each point how strongly the cell contracts in different directions. However, due to its continuum nature, this approach cannot describe situations that depend on the fact that stress fibers are discrete and individual entities, in particular the fact that they can span large distances, that they can cross each other or that they can have very different force-generating capabilities [12].

Because the existence of stress fibers is often related to mechanical challenges, their location typically depends on the geometry of the adhesive environment of the cell, which determines how external forces are transmitted onto cells. While dorsal stress fibers and transverse arcs usually form in the retrograde flow away from advancing cell membranes, ventral and peripheral stress fibers are anchored in focal adhesions that are located behind the leading edge, at the sides or at the back. Thus, their locations strongly depend on the spreading history of the

cell [39, 40]. In contrast to these internal stress fibers that run through the cytoplasm and are believed to be embedded in a weak network of actin filaments, peripheral stress fibers lining the cell contour are closely related to the cell cortex and connect neighboring adhesions by invaginated arcs [13, 14]. Although being contractile and connected to adhesions like ventral stress fibers, these peripheral stress fibers might be differently organized due to their different history [16, 15].

Figure 1(a) summarizes the typical location of ventral and peripheral stress fibers in a schematic drawing for a cell maturely adhering to a substrate. It is assumed that protruding activity important during spreading has already died down. Dorsal stress fibers and transverse arcs are excluded from this drawing because they are believed to contribute less to cell mechanics. In order to study *de novo* generation of stress fibers, one can apply stretching forces to cells, e.g. in a cyclic manner [42, 43, 44]. If in addition one aims at avoiding the effect of surfaces and better mimic the situation in a 3D tissue, one can culture cells in 3D-scaffolds [45, 41, 14, 46]. In Figure 1(b), one example of such a 3D-scaffold is shown as an electron micrograph [41]. The 3D-rendering in Figure 1(c) demonstrates that indeed one can obtain cells with the same geometry as the scaffold, which here is hexagonal. Note that in these experiments, the nucleus tends to be positioned in the middle of the cell, thus excluding a large region of the cells to stress fibers; this is often different in cells adhering to a flat substrate, where the nucleus typically is positioned above a layer of ventral stress fibers. Figure 1(d) shows that in this configuration, the actin cytoskeleton is dominated by peripheral stress fibers forming invaginated arcs, as shown schematically in Figure 1(a) for a cell on a substrate. If one now oscillates one of the microfabricated adhesion platforms with a microindenter, internal stress fibers form in response to the external force, as shown in Figure 1(e). Although the exact mechanisms for their formation in 3D are not known, they are believed to resemble ventral stress fibers, because they are anchored on both sides to strong adhesions. The overlay in Figure 1(f) shows that the newly formed stress fibers follow clear geometrical patterns and one can expect that their biological function would be to protect the cell from mechanical damage, although this is difficult to prove directly.

Here we aim to approach this interesting and important subject from the theoretical side. Motivated by the clear experimental results shown in Figure 1, we suggest a general criterion to predict where such stress fibers appear in cells that are anchored only at a few adhesion sites, one of which is mechanically challenged. In detail, we postulate that stress fibers are generated in such a way as to minimize mechanical stress in the bulk of the cell. At the same time, we also consider that this process should not use too much material, because cytoskeletal resources are limited in cells [47]. Our procedures as explained below lead to a quantitative prediction of the location of stress fibers in whole cells, which is highly relevant both for the basic understanding of cell mechanics and for practical purposes like predicting cell migration in complex environments. It also could contribute to the design of synthetic systems that mimic the mechanical adaptability of living systems, for example for the design of composite material for airplane wings [48]. In order to upscale to whole cells, we are inspired by

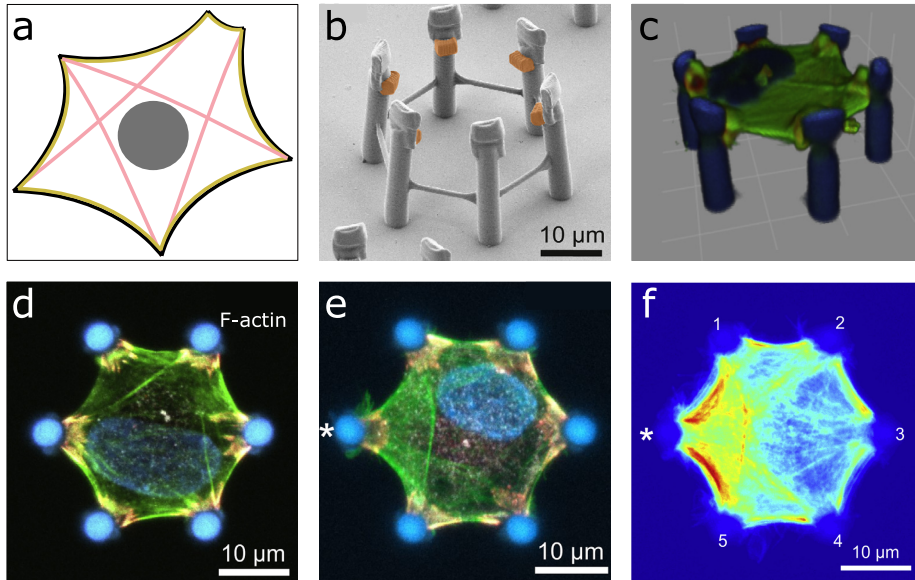


Figure 1: Stress fibers in adherent cells. (a) Cartoon of the stress fiber distribution in a cell adhering to a flat substrate. Peripheral stress fibers (yellow) line the cell contour (black) and in balance with cortical contractility form invaginated arcs. Ventral stress fibers (red) run across the cell in straight lines. (b) To study stress fibers without a large external surface, one can use 3D-printed scaffolds. This scanning electron micrograph shows a hexagonal arrangement to which cells can adhere at the adhesive cubes (orange) 20 μm above ground level. (c) 3D reconstruction of a confocal image stack shows that the cells adhere to the scaffold in a flat, almost planar shape with hexagonal symmetry. (d) Experimental image of a cell adhering in the scaffold. The F-actin signal (green) and the overall cell shape reflect the six-fold symmetry of the scaffold. Peripheral stress fibers are clearly visible together with a few internal ones. (e) Periodic stretching of the left-most pillar (marked with a star) leads to reorganization of actin and the formation of new internal stress fibers. (f) False color plot shows the actin intensity (with red the highest) averaged over ten cells after 15 min of periodic stretching of the left pillar with a frequency of 0.5 Hz and a deflection of 5.3 μm. All experimental images reproduced with permission from [41].

earlier work using FEM-approaches with anisotropic contractions [36, 49]. In contrast to this earlier work, however, here we aim at a FEM-framework that describes single discrete stress fibers to which one can ascribe different properties, reflecting the experimental observation that each stress fiber can be of a different type [12].

In the following, we introduce a model for whole cell mechanics with stress fibers that are described as discrete Euler-Bernoulli (EB) beams embedded into a continuous matrix, similar to finite element models for fiber-reinforced composites [50]. In order to avoid the large computing times required for explicitly resolved stress fibers, we use a recently developed finite element method (CutFEM) [51] that leads to a much reduced computing time. To predict at which positions stress fibers form, we consider different possible measures for internal mechanical stress and then identify integrated von Mises stress as an appropriate choice. We optimize stress fiber distributions using genetic algorithms, because this method fits well to their discrete and modular structure and also allows us to implement resource allocation as a side constraint. The results of our computer simulations are in very good agreement with experiments and thus suggest that the spatial stress fiber configurations found in experiments indeed serve the function of reducing intracellular stress.

## 2 Methods

### 2.1 Linear elasticity

In multicellular organisms, it is a major function of single cells to mechanically contribute to tissue and body shape. Therefore, their effective mechanical laws should contain an elastic element, as evidenced by the stably invaginated arcs in Figure 1. Indeed, whole cell mechanics is often modeled with viscoelastic laws of the Kelvin-Voigt type [52, 49]. Here we focus on the elastic aspect and model the cell bulk as a 2D linear elastic medium in the plane-stress approximation by assuming a flat cell with negligible out-of-plane stress components. In the absence of body force, the problem is then described by the stationary Cauchy momentum equation in two dimensions

$$[\nabla_0 \cdot \boldsymbol{\sigma}(\mathbf{u})] = \mathbf{0}, \quad (1)$$

for the displacement  $\mathbf{u}$ , where  $\nabla_0$  denotes the spatial derivative operator with respect to the undeformed reference (Lagrange) configuration. The Cauchy stress tensor  $\boldsymbol{\sigma}$  is the sum of a passive component  $\boldsymbol{\sigma}_p$  that depends on the displacement  $\mathbf{u}$  and an assumed constant active component  $\boldsymbol{\sigma}_a$ ,

$$\boldsymbol{\sigma}(\mathbf{u}) = \boldsymbol{\sigma}_p(\mathbf{u}) + \boldsymbol{\sigma}_a. \quad (2)$$

The passive component is the usual Cauchy stress tensor for linear elastic materials, defined as

$$\boldsymbol{\sigma}_p = 2\mu\boldsymbol{\epsilon} + \lambda \text{tr}(\boldsymbol{\epsilon})\mathbf{I}. \quad (3)$$

Here  $\lambda$  and  $\mu$  are the Lamé constants,  $\text{tr}$  denotes the matrix trace and  $\mathbf{I}$  is the identity matrix. The linear strain tensor is given by

$$\boldsymbol{\epsilon} = \frac{1}{2} \left[ \nabla_0 \mathbf{u} + [\nabla_0 \mathbf{u}]^T \right] \quad (4)$$

with the superscript  $T$  indicating the matrix or vector transpose. In plane-stress, the Lamé constants are related to the Young's modulus  $E$  and the Poisson ratio  $\nu$  via

$$\lambda = \frac{E\nu}{1-\nu^2}, \quad \mu = \frac{E}{2(1+\nu)}. \quad (5)$$

Performing all calculations per unit length in the third dimension, both Lamé constants have still the units of stress and are measured in Pascal. The active stress component  $\boldsymbol{\sigma}_a$  is the bulk prestress, modeling the myosin motor-induced contraction of the actin network. For simplicity, we here assume an isotropic prestress that is defined by a single parameter  $\varsigma$ ,

$$\boldsymbol{\sigma}_a = \varsigma \mathbf{I}. \quad (6)$$

A positive value,  $\varsigma > 0$ , induces a contraction of the medium and  $\varsigma$  can be thought of as being proportional to the motor density and activity.

## 2.2 Euler-Bernoulli beam theory

For the momentum equation of a 1D Euler-Bernoulli (EB) beam embedded in a 2D medium, we need to decompose the displacement  $\mathbf{u}$  into its normal and tangential components relative to the beam (in contrast to 3D, for 2D we do not need the binormal). With  $\hat{\mathbf{n}}$  and  $\hat{\mathbf{t}}$  being the local normal and tangential unit vectors, these components are given by

$$u_n = \hat{\mathbf{n}} \cdot \mathbf{u}, \quad u_t = \hat{\mathbf{t}} \cdot \mathbf{u}. \quad (7)$$

For the fiber we assume a constant Young's modulus  $E_f$  and a constant radius  $r$ . Since we perform calculations per unit length in the third dimension, the effective cross section is given by  $2r$ . Its momentum equation in the absence of load or body force then reads

$$E_f \frac{(2r)^3}{12} \partial_{tt}^2 \partial_{tt}^2 u_n + 2E_f r \partial_{tt}^2 u_t = 0, \quad (8)$$

where  $\partial_t$  denotes the spatial derivative in tangential direction with definitions

$$\partial_t = \hat{\mathbf{t}} \cdot \nabla_0, \quad \partial_{tt}^2 = \partial_t \partial_t. \quad (9)$$

The first term in Equation (8) describes bending of the beam and the second term contraction/extension.

Because the EB beams serve to represent stress fibers, we have to account for a contractile prestress in tangential direction, due to the action of the myosin

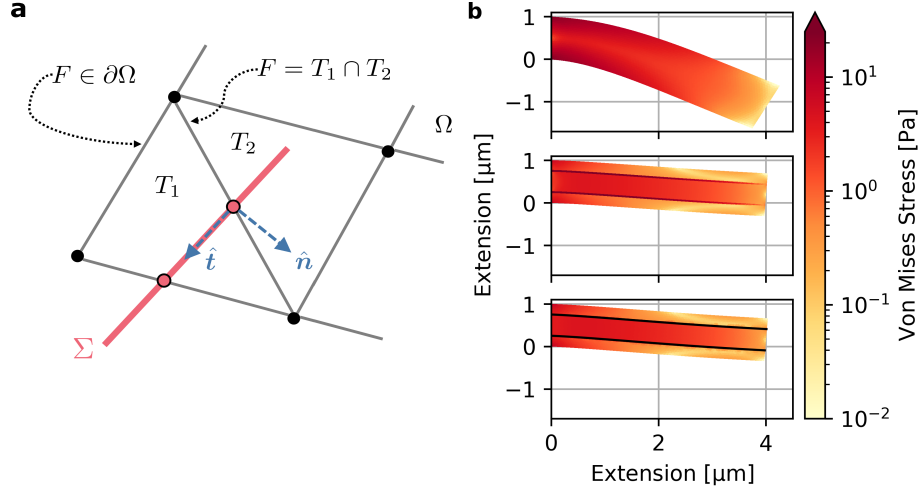


Figure 2: Embedded beam approach using CutFEM. (a) Spatial discretization of the finite element method with embedded beams.  $\Omega \in \mathbb{R}^2$  indicates the modeled two-dimensional elastic domain that is tessellated into grid cells  $T_i$ . The one-dimensional EB beam, given by  $\Sigma$ , is a straight line in the displayed reference configuration with normal vector  $\hat{n}$  and tangential vector  $\hat{t}$ . (b) Bending a composite material under own weight as an example: the structure, with Young’s modulus of 100 Pa and Poisson ratio of 1/3, is fixed at the left side and loaded with a body force of  $-0.4 \text{ Pa } \mu\text{m}^{-1}$  in vertical direction. Top: no EB beams. Middle: two resolved EB beams with a Young’s modulus 100-fold larger than the Young’s modulus of the bulk, same Poisson ratio and a diameter of  $0.05 \mu\text{m}$ . Bottom: two embedded EB beams, indicated by black lines, with the same properties as the resolved ones. The resulting deformation of the structure in the embedded description is the same as in the resolved one.

motors. Similarly to the bulk medium, we assume a prestress parameter  $\varsigma_f$  for fibers, implying

$$\sigma_a = 2r\varsigma_f. \quad (10)$$

Homogeneous contraction should not induce bending, hence the active component only enters the stress contribution in the second term of Equation (8), resulting in

$$E_f \frac{2r^3}{3} \partial_{tt}^2 \partial_{tt}^2 u_n + 2r \partial_t [E_f \partial_t u_t + \varsigma_f] = 0. \quad (11)$$

Again, positive  $\varsigma_f$  corresponds to a contraction of the fiber.

### 2.3 Finite element method

In a first, so-called “resolved” modelling approach, stress fibers are modelled as elastic cylinders with their own Young’s modulus, Poisson ratio and prestress embedded in a bulk medium. In the standard finite element method for linear



elasticity, see e.g. [53], the computational domain is partitioned into mesh elements and the displacement is approximated by a continuous and element-wise polynomial function. An accurate approximation of the stress fibers requires the mesh to resolve them and to be sufficiently fine. Since stress fibers are long, thin objects with a diameter less than one hundredth of the cell diameter, this will lead to a challenging meshing problem, in particular in three spatial dimensions. Moreover, the number and exact location of stress fibers develops dynamically and requires repeated remeshing.

In a second, so-called “embedded beam” modelling approach, the complex (re-)meshing problem is avoided by employing a so-called cut finite element method [54, 55, 51]. Cut-cell methods construct finite element functions on a (simpler) background mesh and then restrict their support to the intersection of the background mesh with the complex domain. A further reduction of complexity can be achieved by representing the stress fibers as one-dimensional straight-line objects of constant thickness in the undeformed domain. In Reference [51], a cut-cell finite element scheme for one-dimensional EB beams embedded in a two-dimensional linear elastic material was developed. We extended this scheme by a prestress term and employ it to model stress fiber systems. The starting point of the scheme in [51] is a standard conforming quadratic finite element method on triangles for two-dimensional linear elasticity equations in displacement formulation of Equation (1). The corresponding conforming triangular mesh constitutes the background mesh for a cut-cell approximation of the fibers, i.e. the mesh is intersected with the straight-line fibers in the undeformed configuration, cf. Figure 2(a), leading to a piecewise quadratic function on line segments for the EB beam formulation. Since Equation (11) is a fourth-order equation in the normal derivatives, a  $C^0$  interior penalty discontinuous Galerkin approach [56] is used to avoid the need for continuity of normal derivatives in the finite element ansatz. As the linear elasticity FEM for the bulk medium and the  $C^0$  interior penalty DG method require the exact same solution spaces, their coupling can be implemented by adding the stiffness matrices of both problems. For the exact formulation of the method we refer to [51].

The finite element scheme has been implemented in the DUNE software framework [57, 58] using its automatic code generation facility [59] to reduce coding effort of the cut-cell scheme significantly. The arising linear systems of equations are solved with the sparse direct solver UMFPACK [60]. Following an example described in [51], Figure 2(b) demonstrates the effect of fibers reinforcing a structure, which is fixed at one side and bends under its own weight. The Young’s modulus of the fibers is 100-fold larger than the one of the bulk. The displacement and bulk von Mises stress (defined in Equation (12)) of the embedded approach agree very well with the resolved description. Before using the embedded beam approach to evaluate complex configurations with many stress fibers, below we will compare the resolved and embedded beam approaches, including prestress and localized external load, to ensure that both approaches produce similar results when representing stress fibers.

## 2.4 Scalar observables for mechanics

As discussed in the introduction, to find locations where stress fibers are generated by the cell, we do not resort to any detailed biophysical model. Rather, we formalize the assumed universal purpose of all stress fibers: they should form to oppose external forces and thus protect the bulk material. Here we propose two scalar quantities to assess the effect of the stress fibers. First, a practical and often used scalar for quantifying stress in a material is the von Mises stress. In the plane-stress approximation, it is given by

$$\sigma_{\text{vM}} = \sqrt{\sigma_{p,xx}^2 - \sigma_{p,xx}\sigma_{p,yy} + \sigma_{p,yy}^2 + 3\sigma_{p,xy}^2}, \quad (12)$$

with the components  $\sigma_{p,ij}$  of the Cauchy stress tensor, given by Equation (3). We do not include the active bulk stress here because it is also a cause of deformations and we aim to minimize their effect. This implies that we consider the undeformed state prior to any deformation due to bulk contraction or external perturbations as our reference state. Because we focus on the passive part of the stress, a similar scalar measure would be the linear strain energy density as expressed via the strain tensor

$$\mathcal{W} = \frac{1}{2}\lambda[\epsilon_{kk}]^2 + \mu[\epsilon_{ij}\epsilon_{ij}], \quad (13)$$

where we use the sum convention for repeated indices. Both quantities are defined at every point of the elastic medium. Note that for both measures we only consider the bulk contributions and do not include the stress or strain within the fibers. In this way, the values of our chosen measures become a function of the fiber characteristics, allowing for an assessment of the protection provided by a fiber configuration of interest.

To define a global loss function, we calculate cell-averaged quantities by integrating over the deformed cell volume  $\Omega$  akin to an  $L^1$ -norm,

$$\|\cdot\| = \int_{\Omega} |\cdot| dV. \quad (14)$$

The task of our optimization algorithm is now to minimize the global mechanical observables  $\|\sigma_{\text{vM}}\|$  and  $\|\mathcal{W}\|$  inside the cell in response to external forces. Note that both quantities have the units of forces instead of energies, since we integrate over a 2D volume.

## 2.5 Genetic algorithm for optimization

Genetic algorithms are used for multi-objective optimization and require only little adaptation to the specific optimization problem at hand [61]. We here employ a variation of the elitist, nondominated sorting genetic algorithm II (NSGA-II) by [62]. Genetic algorithms aim to minimize a set of  $K$  objective functions,

$$\mathbf{z}(\mathbf{x}) = \{z_1(\mathbf{x}), \dots, z_K(\mathbf{x})\}, \quad (15)$$

with respect to a decision variable set,  $\mathbf{x}$ . As the objective functions are usually conflicting, the algorithms optimize according to a domination measure, where

$$\mathbf{x} \prec \mathbf{y}, \text{ if } z_i(\mathbf{x}) \leq z_i(\mathbf{y}) \forall i \in \{1, \dots, K\} \text{ and} \quad (16)$$

$$z_j(\mathbf{x}) < z_j(\mathbf{y}) \text{ for at least one } j \in \{1, \dots, K\}, \quad (17)$$

in which case we say that “ $\mathbf{x}$  dominates  $\mathbf{y}$ .” The set of decision variables that are not dominated by others are considered *Pareto optimal* and form the so-called *Pareto front* in the objective function space. All these configurations are considered as optimal solutions to the problem. In our specific case, a population of decision variable sets corresponds to a certain stress fiber configuration and the objective function can be cell-averaged stress, or elastic energy, and the amount of fiber material.

Each iteration of a genetic algorithm then updates a population of decision variable sets to better resemble the true Pareto front. It applies an update according to a pseudo-evolutionary dynamics, which consists of three steps: (i) *selection* of decision variables whose objective function values are considered closest to the optimal Pareto front, (ii) *crossover* of elements from selected decision variable sets to create “offspring” sets, and (iii) *mutation* of decision variables in the offspring sets. An elitist algorithm preserves variable sets from previous iterations by performing selection simultaneously on the “parent” and on the “offspring” population in each iteration. In the following, we will elucidate the algorithm steps in more detail.

**Selection** Let  $P_t$  denote the parent population and  $Q_t$  denote the offspring population of decision variable sets at algorithm iteration  $t \in \mathbb{N}^+$ . The selection of an elitist genetic algorithm operates on the total population  $R_t = P_t \cup Q_t$ . NSGA-II performs selection by choosing decision variables according to non-dominated fronts and placing them into the new parent population  $P_{t+1}$  until the original parent population size is reached,  $|P_{t+1}| \geq |P_t|$ , where  $|\cdot|$  denotes the set cardinality. A non-dominated front of the full population  $R_t$  is defined as the set of non-dominated decision variable sets,

$$F_i(R_t) = \left\{ \mathbf{x} \in R_t : \mathbf{x} \not\prec \mathbf{y} \forall \mathbf{y} \in R_t \setminus \bigcup_{j=1}^{i-1} F_j \right\}, \quad (18)$$

and the new parent population is the union of these fronts until it reaches the size of the previous parent population,

$$P_{t+1} = \left\{ F_1(R_t), \dots, F_L(R_t) : \left| \bigcup_{i=1}^{L-1} F_i(R_t) \right| < |P_t| \leq \left| \bigcup_{i=1}^L F_i(R_t) \right| \right\}, \quad (19)$$

where  $L$  indicates the number of non-dominated fronts selected. The last selected front typically makes  $P_{t+1}$  larger than  $P_t$ . To ensure a steady size of the parent population, we order the decision variables from the last non-dominated front

$F_L$  by crowding distance, a measure of distance between three adjacent decision variables in objective function space. We then drop the decision variables with the lowest crowding distance score from the new parent population, until its size matches the one of the previous parent population [62].

**Crossover** To create the new offspring population  $Q_{t+1}$ , we repeatedly perform single-point crossover to create two offspring variable sets from two randomly chosen parent variable sets out of  $P_{t+1}$ . The relative probability of a variable set  $\mathbf{x}$  to be selected as parent is given by its fitness

$$f(\mathbf{x}; t + 1) = [\varrho(\mathbf{x}; t + 1)]^{-1}, \quad (20)$$

defined as the inverse of the variable set rank

$$\varrho(\mathbf{x}; t + 1) = 1 + \sum_{\mathbf{y} \in P_{t+1}, \mathbf{y} \prec \mathbf{x}} \varrho(\mathbf{y}), \quad (21)$$

which is one plus the sum of ranks of all variable sets that dominate  $\mathbf{x}$ . This ensures that dominated decision variables receive an escalating rank, implying a lower fitness, and hence a strongly reduced probability of being selected for crossover. Single-point crossover between two selected variable sets  $\mathbf{x}, \mathbf{y} \in P_{t+1}$  then chooses a random crossover index  $i_c \in \{2, \dots, \min(|\mathbf{x}|, |\mathbf{y}|) - 1\}$ , and creates the offspring

$$\mathbf{x}' = (x_1, \dots, x_{i_c}, y_{i_c+1}, \dots, y_{|\mathbf{y}|}), \quad (22)$$

$$\mathbf{y}' = (y_1, \dots, y_{i_c}, x_{i_c+1}, \dots, x_{|\mathbf{x}|}), \quad (23)$$

which become part of the new offspring population  $Q_{t+1}$ .

**Mutation** Variable sets in the new offspring population  $Q_{t+1}$  are then mutated to introduce variation in the population. Mutation of a variable set may include the modification of single or multiple variables in the set, the addition of variables, and the deletion of variables. The exact mechanism strongly depends on the type of optimization problem and the information encoded in the variable sets. Details on the implementation for our specific application to stress fiber configurations are given below.

## 3 Results

### 3.1 Effect of stress fibers on internal cell stress

In Figure 3 we present results for simulations of a contractile cell without and with peripheral stress fibers, using the embedded EBs. In general, we select a hexagonal cell with a circumradius of  $10 \mu\text{m}$  as our reference cell configuration. This shape has the advantage that it is sufficiently detailed to allow the system to develop different responses, but at the same time, its regular geometry gives

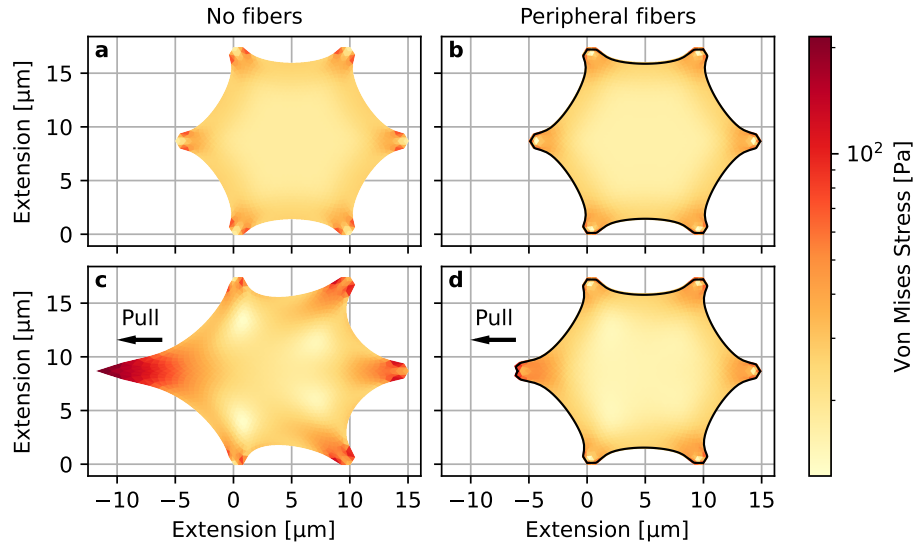


Figure 3: Contractile cell without and with peripheral stress fibers. (a) Simulation of a contractile cell with six adhesion points. We have bulk stiffness of 100 Pa and active stress of 30 Pa, but no stress fibers. (b) Same situation, but now with peripheral stress fibers. The Euler-Bernoulli beams have a stiffness of 10 kPa, a tangential prestress of 1.2 kPa and a radius of 50 nm. (c) Without stress fibers, a force on the leftmost adhesion leads to large von Mises stress in the cell (logarithmic color code). (d) With stress fibers, these large stresses do not develop and the overall displacement is much reduced.

clear results. The corners are assumed to be strongly pinned by focal adhesions, thus we employ a Dirichlet boundary condition on the displacement field there. In contrast, the cell edges are free. This cell is then allowed to contract under its self-generated homogeneous stress  $\sigma_a$ . As seen in Figure 3(a), invaginated arcs form between neighboring adhesions. The presence of peripheral stress fibers in Figure 3(b) does not make a big difference, although a detailed analysis shows that these stress fibers are stretched by 7 percent and that they slightly change the cell shape. In Figure 3(c), we now pull at the leftmost corner. This is achieved by adding a boundary force  $\tau(y)$  using a Neumann boundary condition depending on the vertical extension  $y$ . The force has a maximum of 250 Pa directly at the corner and decreases in  $y$ -direction in a Gaussian shape with a standard deviation of  $0.5 \mu\text{m}$ . One can clearly see that the cell without stress fibers is stretched severely under the action of the force. When now simulating with peripheral stress fibers in Figure 3(d), the internal cell stress is dramatically reduced, demonstrating that stress fibers indeed have a strong role in protecting cells from mechanical challenges.

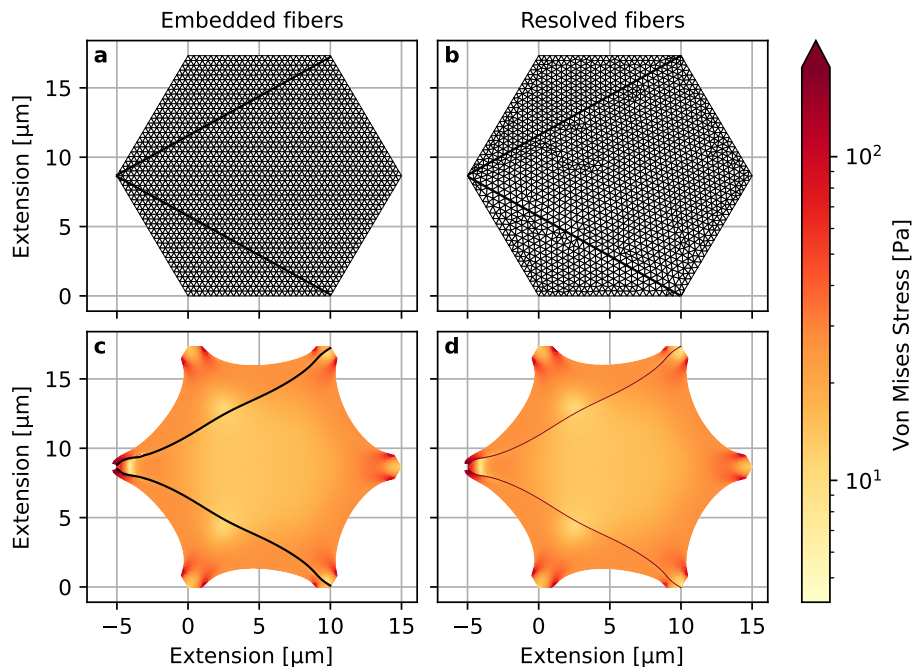


Figure 4: Comparison between embedded and resolved fibers. (a) The grid for embedded fibers does not need any adaptation to the stress fiber (visualized as dark lines, radius not to scale). (b) For resolved fibers, the grid has to be remeshed around the fiber. (c) Simulation of force application to the left corner with embedded fibers, with the von Mises stress color-coded in logarithmic scale. Note that the EB fiber model does not represent the stress inside the fibers. (d) The resolved fiber gives the same result. Now the stress inside the fiber is directly accessible and it is more than one order of magnitude larger than within the bulk of the cell.

### 3.2 Comparing embedded and resolved fibers

In general, stress fibers could occur at any position in the cell and thus we have to check that the CutFEM method also works for more complicated situations. Therefore we next addressed the question of the difference between simulating embedded versus resolved fibers for more complex situations. To that end, we used the same hexagonal cell setup as just discussed. As before, five cell corners were fixed and at the left a force was applied. In Figure 4, we include, as an illustrative configuration, two internal stress fibers with a radius of 50 nm oriented “diagonally” and hence opposing the pulling force towards the left side of the cell. For the EB model, the fibers need not be represented in the grid. Therefore, we create a grid with a Delaunay triangulation only using the hexagonal outline and a target mesh constant of 400 nm, which we have already used in Figure 3. In

contrast, for the explicit representation of the fibers inside the 2D elastic medium, we need to include the fiber geometry into the grid and rerun the triangulation, resulting in a grid with more nodes even though the mesh constant is the same. The resulting grids are displayed in Figure 4(a) and (b), respectively. For the simulations both grids were refined once by subdividing each triangle into four congruent smaller triangles in order to obtain more accurate results and allow for better comparison.

The simulation results shown in Figure 4(c) and (d) used the same parameters as above in Figure 3 and are again color-coded by the von Mises stress. We find that both the cell deformation and the stress distribution in the cell bulk medium calculated by the two methods match almost perfectly. At the left corner, where the force is applied, a subtle difference is notable. The external force acts on several boundary nodes belonging to the explicit fibers, while the contributions of the implicit fibers, in this configuration, are assigned to a single boundary node, which in turn only indirectly “protects” the surrounding ones. This discrepancy becomes smaller the finer the grids are. Note that, in general, small deviations are actually expected, because the explicit fibers are still modelled as an isotropic material, where active contraction occurs also perpendicular to its orientation. That is not the case in the implicit EB model, since we only consider an active prestress in tangential direction, cf. Equation (11).

The region between the fibers right behind the pulled corner is shielded by the two fibers and experiences almost no von Mises stress. The largest stresses appear directly at the pulled edge and at the other corners. The stress inside the fibers in (d) is much higher than in the surrounding medium, ranging up to 1 kPa, and is therefore not represented in the color-code. The EB fiber model considers these stresses as well, but does not explicitly quantify them. In principle, these stresses are accessible in post-processing. However, since we are mainly interested in the stress and strain of the bulk, we do not compute and display the stresses inside the fibers here.

The overall agreement of this comparison demonstrates the validity of the EB model also in the presence of an active prestress and in more complex geometries, extending the analysis of the cut cell FEM method presented in reference [51]. In the context of our work, it is a clear advantage that no remeshing will be necessary as the stress fiber distribution changes.

### 3.3 Effect of changing stress fibers

Next we addressed the question how changing positioning and length of stress fibers affects the stress distribution inside cells. These investigations are also helpful to decide which optimization principle is most appropriate in our context. We start by defining different types of stress fibers in our implementation, motivated also by the experimental observations of stress fibers described in the introduction. Figure 5(a) displays these distinct configurations, labeled as follows:

- *Side*: The two fibers (blue in Figure 5(a)) in direct contact to where the

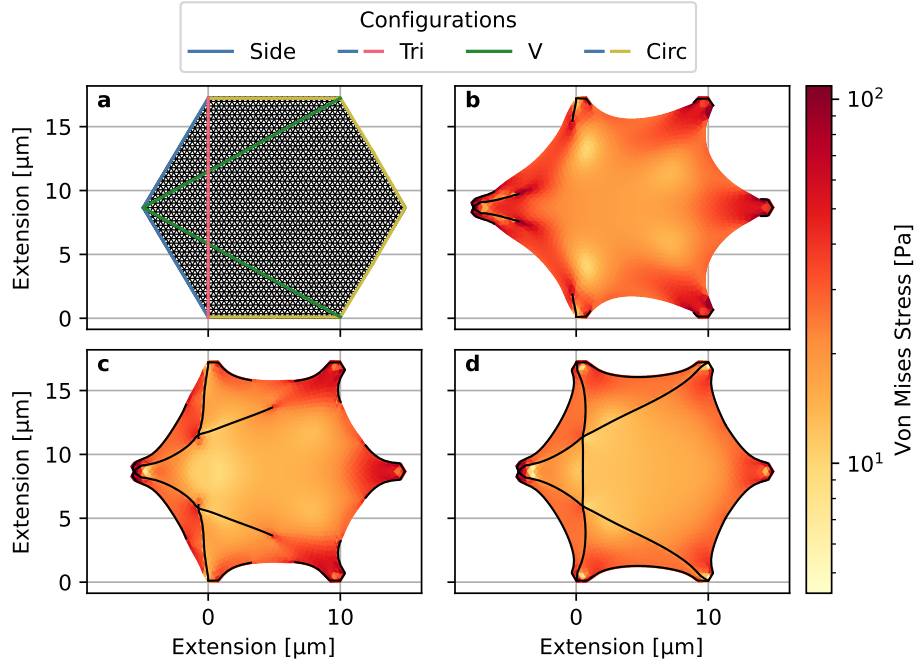


Figure 5: Effect of different fiber types and lengths. (a) We consider four different fiber configurations based on experimental observations. (b)-(d) Simulation results for quasi-static growth at different fiber lengths of (b) 30 %, (c) 60 % and (d) 100 % of the final length. The von Mises stress is represented by the color-code in logarithmic scale.

force is applied

- *Tri*: The fibers of *Side* together with a vertical fiber (red) connecting the former
- *V*: The two diagonal fibers (green), already studied in Figure 4, connecting the point of force with the right corners.
- *Circ*: All peripheral fibers, as already studied in Figure 3, including the ones of *Side*
- *All*: All fibers from the four configurations above.

Since we are only interested in the steady state distributions of stress fibers and not in their dynamics, we simulated fiber growth by computing stationary solutions for configurations with fiber segments of varying length, chosen from the families above. Except for the fibers of the *Side* and *V* configurations, where the force is directly applied at one of the starting points of the fiber, we let fibers grow from both attachment points symmetrically and meet at the center, see



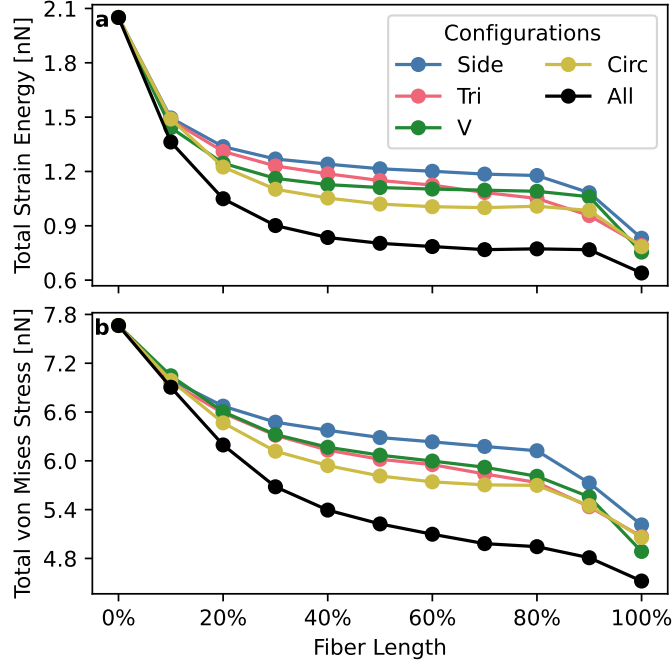


Figure 6: Scalar measures for internal cell stress. (a) Integrated strain energy and (b) integrated von Mises stress as functions of the stress fiber extension for the different fiber configurations.

Figure 5(b)-(d). The material properties and boundary conditions were chosen as in the previous section.

The effect of the fiber growth on the mechanics was investigated by calculating the integrated von Mises stress  $\|\sigma_{vM}\|$  and the integrated energy density  $\|\mathcal{W}\|$ , as displayed in Figure 6. This shows that both quantities are maximal when there are no stress fibers in the cell. As the stress fibers grow, the von Mises stress monotonously decreases and reaches a boundary minimum for fully elongated stress fibers for all fiber configurations. As expected, all four configurations together (*All*) result in the lowest stress for all fiber lengths. The *Circ* configuration has the largest contribution in stress reduction for not fully extended fibers, while at the end the *V* configuration with only two fibers outperforms *Circ*. In addition, *Side*, as a part of *Circ*, almost leads to the same final von Mises stress as *Circ*, indicating that the fibers close to the pulled corner are the most important and, as already observed in Figure 3, stretching is more relevant than bending.

Interestingly, in contrast to this simple behavior of the von Mises stress, the strain energy remains, after an initial drop, mostly constant for increasing fiber length and is only dropping again when fibers are fully extended. Notably, the energy minimum may not be reached for a given fiber configuration, which

could lead to suboptimal results in the optimization process. These observations suggest that the von Mises stress is a more suitable objective function due to its monotonous behavior and the better performance of fibers, which directly oppose the external force.

### 3.4 An optimization scheme for fiber distribution

We now define an optimization scheme for finding stress fiber configurations in a cell based only on mechanical parameters and solve it using a genetic algorithm as introduced in section 2.5. Building on the simulation setup discussed in the previous section, we choose the placement and radii of the stress fibers as decision variables. The component of a decision variable  $x_i \in \mathbf{x}$  is then a set of two coordinates  $\mathbf{p}_i^{(1)}, \mathbf{p}_i^{(2)}$ , which give the start and end position of the fiber  $i$ , respectively, as well as the fiber's radius  $r_i$ ,

$$x_i = \left\{ \mathbf{p}_i^{(1)}, \mathbf{p}_i^{(2)}, r_i \right\}. \quad (24)$$

The decision variable then is a  $N$ -tuple of these,

$$\mathbf{x} = (x_1, \dots, x_N), \quad N \in \{N_{\min}, \dots, N_{\max}\}. \quad (25)$$

The total number of stress fibers in a cell varies, both between cell types and the given situation. We choose the minimum number of stress fibers as  $N_{\min} = 3$  and the maximum as  $N_{\max} = 30$ , in addition to the six peripheral fibers called *Circ* in the previous section.

As discussed in the introduction and investigated for the specific fiber positions in the last section, we assume that the stress fiber configuration aims to minimize the overall stress in the cell, while in addition using as little material as possible. Ignoring the underlying biochemical signalling and assembly processes, this suggests two objective functions. First, the total von Mises stress,

$$z_1(\mathbf{x}) := \|\sigma_{\text{vM}}\|, \quad (26)$$

which technically is not a function of  $\mathbf{x}$ , but computed from the elasticity model of the cell including the fibers encoded by  $\mathbf{x}$ . And second, the total volume, here in two dimensions the total area, respectively, of the stress fibers,

$$z_2(\mathbf{x}) := \sum_{i=1}^N 2r_i \left\| \mathbf{p}_i^{(1)} - \mathbf{p}_i^{(2)} \right\|_2, \quad (27)$$

where  $\|\cdot\|_2$  indicates the usual Euclidean vector norm.

We chose a parent and offspring population size of 200,  $|P_t| = |Q_t| = 200$ . The initial population  $Q_1$  consists just of random fiber configurations. Specifically, it is created by choosing a random number of fibers  $N$  from a uniform distribution,  $N \sim \mathcal{U}(N_{\min}, N_{\max})$ , for each decision variable, and then selecting two random, uniformly distributed points inside the 2D grid and a random radius from a normal distribution,  $R \sim \mathcal{N}(\mu = 50 \text{ nm}, \sigma = 15 \text{ nm})$ , for each fiber. The two

points define a line which is extended until the start and end points,  $\mathbf{p}^{(1)}$  and  $\mathbf{p}^{(2)}$ , are close to the grid boundary (i.e. the cell membrane).

Selection is trivial in the first iteration, as all initial population members are selected,  $P_1 = \emptyset, P_2 = Q_1$ . However, the process is still required to determine the rank and hence fitness for each initial decision variable in order to subsequently apply crossover. After selection of the parent population  $P_t$ , we apply crossover to create an offspring population  $Q_t$ , as presented in section 2.5. Crossover is stopped when the offspring population size equals 90% of the parent population size. The remainder of the offspring population is filled up again by random fiber configurations as outlined above. We introduce this procedure to the NSGA-II algorithm in order to ensure a sufficient randomness of not only single fibers but also entire fiber configurations.

The offspring population is then mutated by iterating over every decision variable  $\mathbf{x} \in Q_t$  and performing the following alteration steps:

1. *Removal* of a randomly chosen fiber with probability  $p_r = 0.7$ , if  $|\mathbf{x}| > N_{\min}$ .
2. *Variation* of fibers with probability  $p_v = 0.7$  for each fiber, by drawing new fiber coordinates and radii from normal distributions whose mean is given by the respective current value. This effectively implements a random walk of the single fiber parameters,

$$\mathbf{p}_i^{(j)'} \sim \mathcal{N}\left(\boldsymbol{\mu} = \mathbf{p}_i^{(j)}, \boldsymbol{\Sigma} = [400 \text{ nm}]^2 \mathbf{I}\right), \quad (28)$$

$$r_i' \sim \mathcal{N}(\mu = r_i, \sigma = 15 \text{ nm}), \quad (29)$$

where the dashed quantities indicate the parameters after variation and  $\mathcal{N}(\boldsymbol{\mu}, \boldsymbol{\Sigma})$  is a multivariate normal distribution with mean  $\boldsymbol{\mu}$  and covariance matrix  $\boldsymbol{\Sigma}$ ,  $\mathbf{I}$  the identity.

3. *Addition* of one fiber with probability  $p_a = 0.7$ , if  $|\mathbf{x}| < N_{\max}$ . With an additional probability of  $p_s = 0.8$ , the placement of the new fiber is not random but chosen according to local maxima in the von Mises stress distribution. For this, one local maximum is selected with a relative probability of  $p = \sqrt{\sigma_{\text{vM}}}$ , with  $\sigma_{\text{vM}}$  the von Mises stress of the local maximum. The position of the selected maximum is used as center point of the new fiber, and the direction of the fiber is determined along the direction of the principal stress component at this location. Again, the fiber is then extended in both directions until the start and end points lie sufficiently close to the grid boundary.

After mutation, the entries of each decision variable are shuffled.

Finally, the fiber configuration defined by each decision variable of the new offspring population is inserted into the elasticity model and the first objective function, i.e. the overall stress Equation (26), is calculated. The second objective function, the total stress fiber volume, Equation (27), is computed directly from the decision variables. Because we focus only on internal fibers, which form during mechanical challenges, the peripheral fibers are excluded from the genetic

Table 1: Parameters used in the genetic algorithm.

Topic	Quantity	Value	Unit
Cell bulk medium (cytoplasm)	Young’s modulus	100	Pa
	Poisson ratio	1/3	
	Isotropic prestress	30	Pa
Stress fibers	Young’s modulus	10	kPa
	Tangential prestress	1.2	kPa
	Initial mean radius	50	nm
	standard deviation (SD) of radius	15	nm
Mutation parameters	Fiber removal prob. $p_r$	0.7	
	Fiber variation prob. $p_v$	0.7	
	SD of fiber start/end translation	400	nm
	Fiber addition prob. $p_a$	0.7	
	Prob. for stress-aligned fiber placement $p_s$	0.8	
Nucleus bulk medium	Young’s modulus	1	kPa
	Poisson ratio	1/3	
	Isotropic prestress	0	Pa

algorithm and do not contribute to the computation of the total fiber volume through objective function  $z_2$ .

As a model refinement, we also investigate the effect of the cell’s nucleus on the stress fiber configurations computed by the genetic algorithm. The nucleus is implemented as an elastic material in the center of the grid with different material properties. In the reference configuration, the nucleus is round with a radius of 3  $\mu\text{m}$ . The reference grid was adjusted such that grid element interfaces coincide with the nucleus outline. The nucleus bulk material is chosen to be ten times stiffer than the surrounding cytoplasm [63, 64], with a Young’s modulus of  $E = 1 \text{ kPa}$  and Poisson ratio 1/3. Since the contractile stress originates from the cytoskeleton, which is excluded from the nucleus, we assume the isotropic prestress to be zero within the nucleus. The fiber placement by the genetic algorithm has now to be slightly adapted to avoid fibers passing through the nucleus. To that end, the stress-based placement iteratively selects local stress maxima based on their relative probability, as outlined above, until the resulting fiber will not pass through the nucleus. If this is not the case for any local stress maximum, the algorithm will go back to placing a random fiber instead. The random fiber placement, in turn, generates random fibers as outlined above, until the created fiber will not pass through the nucleus. Table 1 summarizes all parameters used in the elastic model and the genetic algorithm.

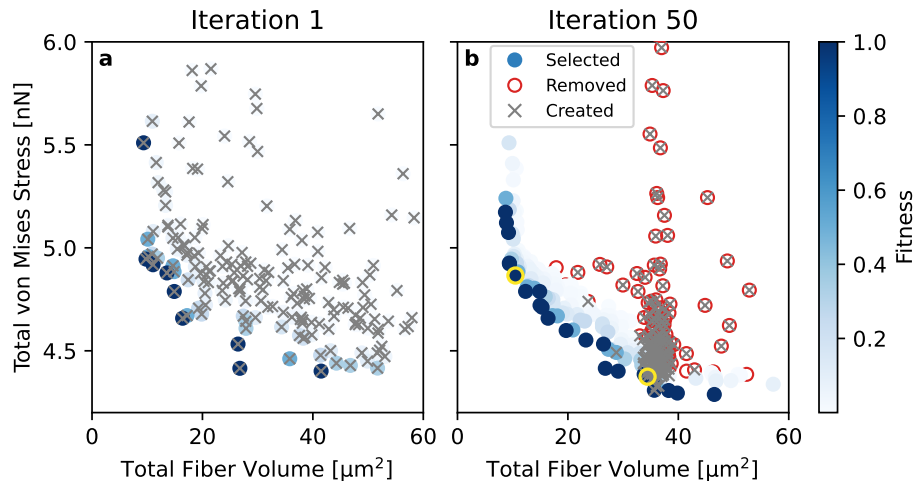


Figure 7: The objective function space with overall stress  $z_1(\mathbf{x})$  and stress fiber volume  $z_2(\mathbf{x})$  of the genetic algorithm with decision variables  $\mathbf{x} \in R_t = P_t \cup Q_t$  for (a) iteration  $t = 1$  and (b) iteration  $t = 50$  after selection was applied. Blue markers denote selected decision variables  $\mathbf{x} \in P_{t+1}$ , with the color indicating the respective fitness value  $f(\mathbf{x}; t+1)$ . Red circles denote variables that were not selected and hence removed from the population. A cross additionally indicates variables  $\mathbf{x} \in Q_t$  that were created in the respective iteration and thus are part of the most recent offspring population. Note that in the first iteration no decision variables are removed, as no parent population exists yet. The corresponding cell elasticity models of the two configurations marked by yellow outlines in (b) are displayed in Figure 8.

### 3.5 Optimal fiber distributions

To demonstrate how the optimization process works, Figure 7 displays the objective function space for all decision variables  $\mathbf{x} \in R_t = P_t + Q_t$  at the beginning (after just one iteration) and after 50 iterations of the genetic algorithm. We find that the overall stress, indicated by  $z_1(\mathbf{x})$  on the ordinate, generally decreases with increasing stress fiber volume,  $z_2(\mathbf{x})$  on the abscissa. The Pareto front is convex in objective function space, and its sampling improves with the algorithm iterations, cf. Figure 7(a) vs. (b). While the initial spread is large, after several iterations most decision variables lie close to the non-dominated front. As can be seen by the coloring in Figure 7(b), the algorithm usually creates an offspring population that is localized in objective function space, and discards most of these decision variables immediately (cf. the red circles).

Figure 8 displays results for the cell elasticity model for two decision variables from the non-dominated front shown in Figure 7(b) (denoted there by the yellow circles). They visualize the (near) extrema of the non-dominated front by optimizing the configuration for either (a) large stress and low total fiber

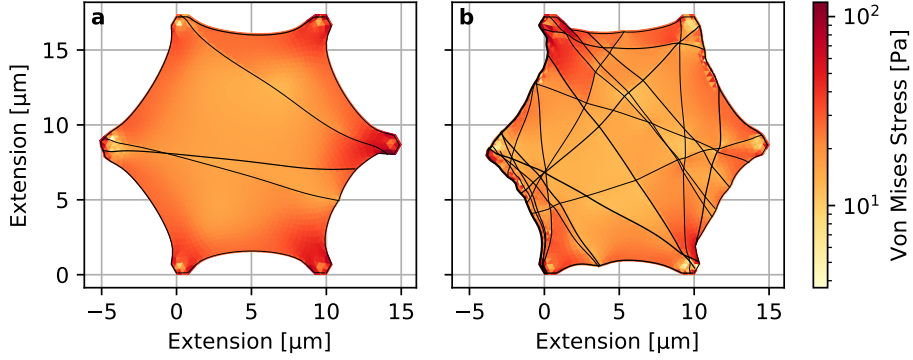


Figure 8: Two exemplary fiber configurations in the non-dominated front of the genetic algorithm after 50 iterations. Fibers are drawn as black lines whose line width indicates the fiber radius (not drawn to scale). Fiber radii in both configurations range from 18 nm to 113 nm. (a) Low fiber material consumption ( $z_2 = 10.49 \mu\text{m}^2$ ) but relatively large stress ( $z_1 = 4.87 \text{nN}$ ), also visible by the greater displacement to the left of the pulled corner. (b) Reduced stress ( $z_1 = 4.37 \text{nN}$ ) at the cost of using a lot more fiber material ( $z_2 = 34.43 \mu\text{m}^2$ ).

volume or (b) low stress with large total fiber volume. The configuration shown in (b) reaches an overall stress of  $\|\sigma_{\text{vM}}\| = 4.37 \text{nN}$ , compared to  $4.87 \text{nN}$  for configuration (a). However, the total fiber volume required by configuration (b) is more than three times larger than that of (a), with  $z_2 = 34.43 \mu\text{m}^2$  (b) against  $10.49 \mu\text{m}^2$  (a).

To evaluate and visualize also the resulting whole population of stress fiber configurations, we select the configurations with a fitness of one and call them population  $O_t$ , which typically is here of the size of around 10% of the whole population. We investigate the relative stress fiber density per grid element  $T$ , given by

$$\rho_T = \frac{1}{\max_T \rho_T} \sum_{\mathbf{x} \in O_t} \sum_{i \in \mathcal{I}(\mathbf{x}, T)} 2r_{\mathbf{x}, i}, \quad (30)$$

where  $\mathcal{I}(\mathbf{x}, T)$  collects the indices of fibers in  $\mathbf{x}$  passing through grid element  $T$ , and  $r_{\mathbf{x}, i}$  is the radius of the fiber with index  $i$  in  $\mathbf{x}$ .

This relative stress fiber density is visualized in Figure 9 over the mean displaced geometry of all  $\mathbf{x} \in O_t$  for iteration (a)  $t = 10$  and (b)  $t = 50$ . One can clearly see that the density distribution is non-symmetric, reflecting the effects of the force applied to the left, although the initial geometry is symmetric. The highest stress fiber density is found at the peripheral arcs of the left side. Stress fibers running through the cell tend to have at least one of their start or end points near an attached corner of the cell. Fibers also appear to form nearly parallel groups. After 50 iterations, we find that diagonal fibers, similar to the  $V$  configuration in Figure 5, are more prevalent than single horizontal fiber in the center that would directly oppose the exerted force.

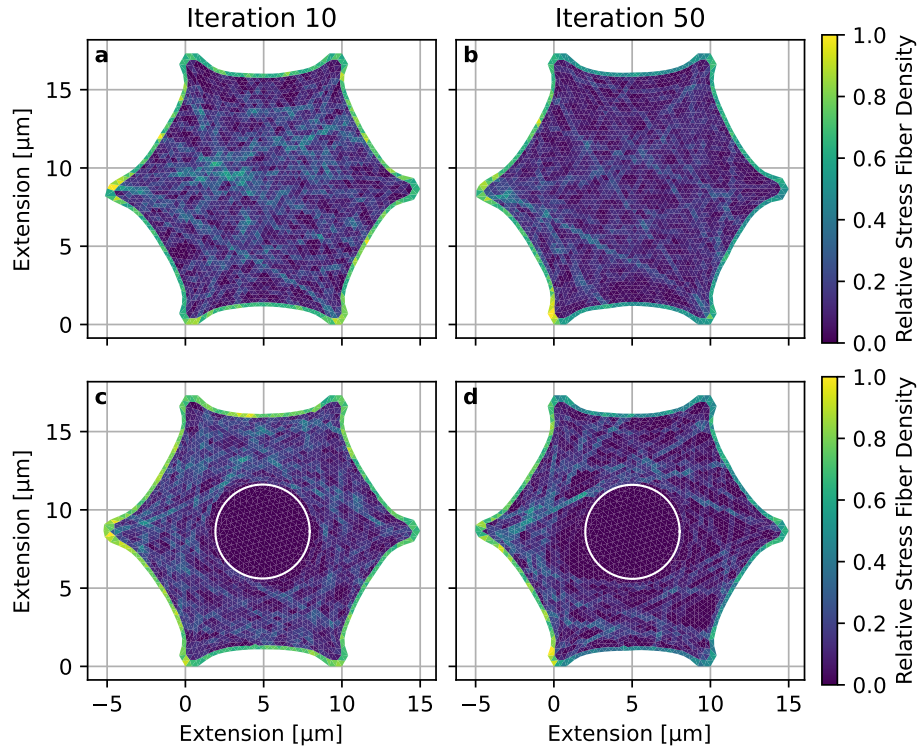


Figure 9: Relative stress fiber density averaged over all configurations with a fitness of one. The geometry is given by the mean displacement of these configurations. (a) After 10 and (b) after 50 iterations of the genetic algorithm. (c) and (d) show the same simulations as (a) and (b), respectively, but now in the presence of an initially round nucleus in the cell center (outline indicated by white circle), through which stress fibers are not allowed to pass.

To be even closer to the experimental situation, we study the same setup including the cell's nucleus, as explained in the previous section. Figure 9(c) and (d) display the relative stress fiber density, for iteration  $t = 10$  and  $t = 50$ , to be directly comparable to (a) and (b) in the absence of the nucleus. A  $V$  configuration starts to form after 10 iterations and is clearly visible after 50 iterations, as anticipated by the exclusion effect of the nucleus. As already observed without a nucleus, the peripheral fibers at the left side are strongly enhanced compared to the other four. Together with vertical fibers connecting the two attached corners left to the nucleus, these peripheral fibers form the *Tri* configuration, the importance of which we already found in Figure 6 and which is also observed in experiments, cf. Figure 1(f). Overall, at  $t = 50$ , the entire population shows a broken symmetry similar to the single configuration in the Figure 8(b), reinforcing the left side.

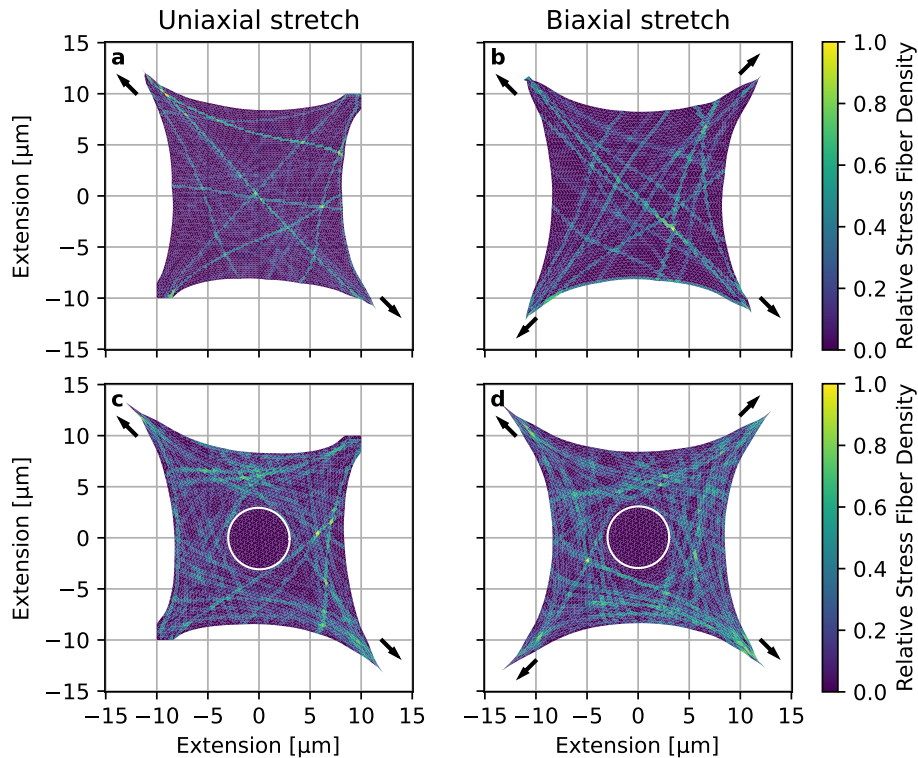


Figure 10: Relative stress fiber density averaged over all configurations with a fitness of one after 50 iteration of the genetic algorithm for stretching a square-shaped cell, where the arrows indicate the direction of applied force. The average is taken over all configurations with a fitness of one and the geometry is given by the mean displacement of these configurations. (a) Uniaxial and (b) biaxial stretch without a nucleus. (c) Uniaxial and (d) biaxial stretch in the presence of an initially round nucleus (outline indicated by white circle) in the cell center, through which stress fibers are not allowed to pass.

To demonstrate that our optimization procedure is generally applicable to different geometries and external force conditions, we also investigate uni- and biaxial stretching of a quadratic cell. We use the exact same values of the mechanical and optimization parameters as before (cf. Table 1). The resulting fiber distributions are shown in Figure 10, in (a) and (b) without a nucleus and in (c) and (d) with a nucleus, respectively. Without a nucleus, fibers form predominantly along the directions of the applied force (indicated by black arrows) and run from one to the opposite corner, as one would expect and has been observed experimentally for cells on substrates under static stretch [65]. Note that our discrete approach allows for solutions in which the stress fibers cross each other. This stands in marked contrast to continuum descriptions of



local actin orientation, which would predict vanishing orientation at the crossing points [36, 66, 67]. In the uniaxial case, almost all other prominent fibers are anchored at least at one end to a Dirichlet boundary condition, i.e. to a focal adhesion, forming  $V$ -shaped configurations, which we have already observed in the previous hexagonal setup. These  $V$  configurations are the main feature in the presence of a nucleus (Figure 10(c) and (d)), since then fibers cannot run between opposite corners anymore. The overall stress fiber distribution changes drastically, leading to a slightly less efficient reinforcement such that a little bit more fiber material is needed to reduce stress by the same amount. This is also reflected in the larger average displacement in Figure 10(b) and (d) compared to (a) and (c), respectively. Thus, also in real cells the nucleus might present an important geometrical challenge depending on the geometry of the attachment points and focal adhesions. However, most of the fibers are still anchored to one of the stretched corners and are able to reduce displacement and therefore stress substantially compared to a situation without any fibers. In 4, the predicted fiber distribution of a sheared cell is shown as another example.

## 4 Discussion

In this work, we have presented a novel approach to simulate the mechanics of biological cells with contractile actin stress fibers. We modeled the fibers as prestressed, one-dimensional Euler-Bernoulli (EB) beams embedded in a bulk elastic medium using the CutFEM method developed by [51]. Our simulations of stress fiber positioning after mechanical stimulation show very good agreement with the experimental observations reported by [41], demonstrating that these configurations minimize internal mechanical stress. As a measure for this stress, we used the  $L^1$ -norm of the von Mises stress in the bulk. The optimization procedure was implemented with genetic algorithms, minimizing both the stress and the amount of actin used for stress fibers in the cell. Our work demonstrates that typical stress fiber structures within cells can be predicted by focusing on mechanics and not considering biochemical details.

A central element of our work is the requirement to efficiently simulate the effect of stress fibers. Here we use the recently introduced method of CutFEM [51] for embedded fibers. Our simulations in section 3.2 demonstrate that modelling cellular stress fibers as EB beams with prestress via CutFEM is in very good agreement with simulating the fibers explicitly. Only slight differences are visible near the cell boundary and at the end of fibers due to the singular character of the 1D fibers, see Figure 4. Employing finer meshes or local mesh refinement around the ends of the fibers reduces these effects.

The main advantage of the EB model is that the fiber configuration is independent of the bulk material grid. Especially when many fibers are simulated, the generation of a grid that needs to explicitly resolve all fibers can be tedious or must be automated. Even so, the number of grid nodes, and hence the computational cost, rises strongly with the number of fibers because their diameters (100 nm) are small compared to the extensions of a cell (10  $\mu$ m). The

EB model therefore enabled us to compute solutions for numerous stress fiber configurations based on very few grid files, and to automate this process when using the genetic algorithm. In the future, it would be very interesting to extend this procedure from 2D to 3D situations, especially for experimental situations in which cells are not in the effectively 2D situation shown in Figure 1. As a downside, the discontinuous Galerkin formulation of the model by [51] is difficult to implement, mostly due to the geometric transformations required to compute the normal and tangential derivatives.

Linear elasticity as used here is only a first-order approximation for the complex mechanics of cells [68, 69]. A more detailed approach might consider the non-linear elasticity that emerges for networks of semiflexible polymer networks as the cytoskeleton [70]. In principle, our approach can be extended to nonlinear elasticity in the future, as the bulk elasticity and the fiber model couple only through the common displacement field. This fact in particular enables the presented linear EB model to be combined with a non-linear model for bulk elasticity.

Our approach also simplifies several features of actin stress fibers. In adherent cells, stress fibers are often anchored by focal adhesions, which connect them to the extracellular matrix [11]. It is less clear how their ends are organized if not anchored to adhesions. In our model, fibers are allowed to end at any point inside the cell. As special anchoring points are not considered, the fiber (pre)stress must then be compensated by the elastic medium surrounding the fiber end. Since the Young’s modulus of the fiber exceeds the one of the bulk medium by several orders of magnitude, this can lead to non-physical solutions where the bulk medium folds in on itself, an effect that could be avoided by implementing explicit anchoring points. We also assume that a bulk elasticity model based on finite strain theory might alleviate this issue.

For simplicity, we considered only homogeneous fibers, i.e. with constant stiffness and radius. It has been shown in [71] that stress fibers can appear heterogeneous towards strong contractile levels, and mechanically non-linear towards weak contractile levels. While heterogeneity is conceptually included in EB beam theory and could be directly studied with the approach reported here, beam nonlinearity is not and would require additional modeling efforts.

Our simulations in section 3.3 demonstrate that fiber configurations observed in experiments reduce the stress in the cell, both individually and jointly. We have found the global von Mises stress  $\|\sigma_{\text{vM}}\|$  to be a good quantification of the overall cell stress, as it decreases monotonically for increasing fiber lengths and reaches a minimum when all fiber configurations found in experiments are combined. In contrast, the global strain energy  $\|\mathcal{W}\|$  is not strictly decreasing with fiber length and therefore less suitable. In the future, one could identify other measures of internal cell stress that work well, including contractions of higher order tensors representing network organization.

The genetic algorithm of section 3.4 produces stress fiber configurations that resemble those found in experimental studies. This demonstrates that it is feasible to define the problem of finding optimal fiber configurations as a multi-objective optimization task, where both the stress in the cell and the

amount of actin used to build stress fibers are sought to be minimized. Our approach ignores underlying biochemical mechanisms and operates only on a cell-macroscopic mechanical level. Our results serve as a proof of concept, indicating that modeling biochemical mechanisms within the cell are not necessarily required when investigating the formation and configuration of stress fibers, especially when focusing on their mechanical aspects.

Testing our algorithm with the same optimization parameters for a different cell geometry for uni- and biaxial stretching as well as for shear forces (see 4) again resulted in realistic fiber configurations. In particular, our algorithm predicts that discrete stress fibers can cross each other, which is a remarkable result that cannot occur in a continuum theory. This validates our hypothesis of global stress minimization and demonstrates the applicability of the optimization procedure without additional adaptation to the specific problem. A nucleus representing an excluded volume, which cannot be intersected by the fibers, can change the resulting fiber distribution substantially. Depending on the geometry of the investigated problems, it might hinder the formation of very effective fibers, like in the case of uni- and biaxial stretching, or it singles out a very distinct fiber configuration from a former more homogeneous distribution. In the future, our purely mechanical approach could be complemented by biochemical aspects, including signaling through the Rho-system, which is the main regulator of contractile actin architectures [2, 72, 49].

Our approach is mainly phenomenological, as it focuses on few global parameters in the mechanical system of the cell. It is clear that biological cells do not actively solve an optimization problem like the one we implemented. They have a limited actin pool to build stress fibers from and are unable to sense a global quantity like the von Mises stress  $\|\sigma_{vM}\|$ . However, they are able to sense local stress via mechanosensing pathways that trigger actin condensation and subsequently form actin strands in the direction of principal stress. As the actin filaments have a much higher stiffness than the cellular cytoplasm, the filament formation reduces stress in the cytoplasm. Active stress fiber contraction then also decreases strain if it is able to counteract the force exerted on the cell. These mechanisms contribute to a decrease in stress and strain throughout the cell and we therefore deem  $\|\sigma_{vM}\|$  a sensible global measure albeit originating from a local biochemical-mechanical interplay.

Our study reported here is not exhaustive and the optimization process could be further improved to possibly yield results that are more consistent and closer to reality. Our current implementation performed optimization by changing fiber positions and fiber radii. Other fiber parameters like Young's modulus and prestress could also be added to the genetic algorithm. In principle, one would expect stiffer fibers without prestress could oppose an external stretching force equally well as a softer, prestressed fiber. However, to reduce the overall displacement about the same amount under the same conditions, the stiffness would have to be increased more than twofold in our simulations, which would not be in the physiological range of real stress fibers. Furthermore, prestressed fibers in the wrong place might increase displacement of the bulk unnecessarily and increase stress drastically if their ends are not anchored to focal adhesions.

Therefore, prestress facilitates the efficient placing of fibers. Without fiber prestress, the resulting fiber distribution obtained with our genetic optimization qualitatively differs from the here shown results in Figure 9 with prestress and reproduces the experimental images less well. If verified experimentally, predictions for these parameters would provide valuable information because assessing fiber parameters *in vitro* is still difficult. Also note that due to a small total fiber number – which however is realistic for cells – the results produced by the current genetic algorithm depend on the generation of random numbers. Fiber configurations can vary strongly between different runs with the same parameters but different seeds. Most resulting populations are dominated by few fiber configurations, which might be remedied by a higher population size. However, even though a single run of the genetic algorithm does not necessarily explore all fiber configurations found in experiments, we find that it samples the objective function space well, cf. Figure 7. Therefore, the used population size is sufficient to obtain good agreement with the averaged experimental fiber distribution. The genetic algorithm has a low acceptance rate, meaning that only few configurations from offspring populations are actually selected in the next iteration. This is the reason why we chose an elitist algorithm in the first place. Single point crossover between Pareto-optimal configurations seems to produce mostly inferior configurations in our case. We conclude that the underlying assumption of the genetic algorithm, namely that fibers in a decision variable are independent, may not be truly justified. In principle this is intuitive: Any fiber that does not run along the symmetry axis of the problem (in the hexagonal setup, the horizontal) needs a symmetric counterpart to avoid deformation into its direction. Our implementation so far neglects these relations between fibers within a configuration. A significant improvement for a fiber configuration search algorithm would be to consider such beneficial correlations between fibers. It could then perform an optimization based on structures consisting of multiple fibers like the ones we investigated in section 3.3. Presumably, a machine-learning algorithm would be better suited for such a task than a genetic algorithm.

Finally, as we have formulated an optimization problem based mostly on fiber positioning, transient aspects of fiber creation are not considered in this approach. As actin polymerization and myosin II contractility in cells is locally initiated in regions in which stress is high, the fiber distribution in real cells necessarily depends on the dynamics of this process. It would be interesting to also study these aspects of fiber growth in the future.

## Data accessibility

Our computer code is publicly available at <https://github.com/usschwarz/dune-structures>.

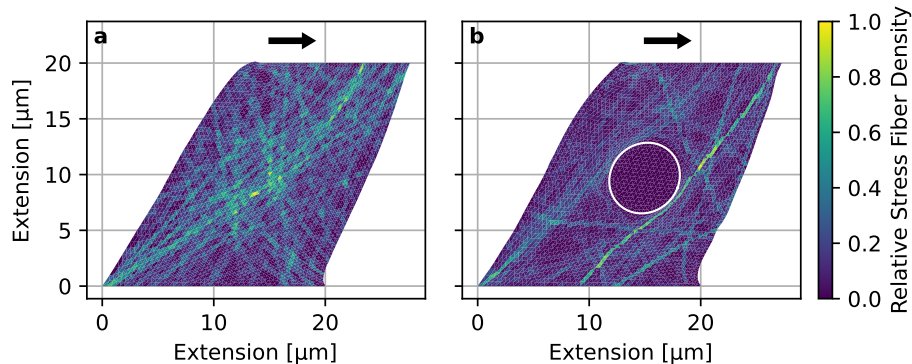


Figure 11: Relative stress fiber density averaged over all configurations with a fitness of one after 40 iteration of the genetic algorithm for shearing a square-shaped cell, where the arrows indicate the direction of applied force, while the cell's position is fixed at the bottom as well as the height in vertical direction. The average is taken over all configurations with a fitness of one and the geometry is given by the mean displacement of these configurations. (a) Without a nucleus and (b) in the presence of an initially round nucleus (outline indicated by white circle) in the cell center, through which stress fibers are not allowed to pass.

## Authors' contributions

All authors contributed to the conceptualization of this work. LR, VW and DK performed the work and implemented the code. All authors analyzed and discussed the simulation results. PB and USS supervised the projected and acquired funding. LR and USS wrote the original draft. All authors reviewed and commented on the text.

## Conflict of interest declaration

We declare that we have no competing interests.

## Funding

This work is funded by Deutsche Forschungsgemeinschaft (DFG, German Research Foundation) under Germany's Excellence Strategy - EXC 2181/1 - 390900948 (the Heidelberg STRUCTURES Excellence Cluster).

## Appendix: Optimal fiber distribution of a sheared cell

To test our algorithm in a slightly different, less structured setting, we consider a initially square-shaped cell, which is attached to a substrate along the whole length of one edge, instead of discrete anchoring points investigated in section 3.5. When then apply a force, parallel to the substrate, at the top of the cell to shear it, while keeping its height fixed. In figure 11 the resulting fiber distribution of our genetic algorithm is shown after 40 iterations. In (a), without a nucleus, fibers mainly form from the lower left to the upper right corner to oppose the external force, while being anchored to the substrate. In general, fibers tend to run from the bottom to the top, as one would expect. In the presence of a nucleus, which cannot be crossed by the fibers, two main fibers, running vertically on the left and right side of the nucleus, emerge. As observed before, the nucleus hinders the most efficient fiber formation and more fiber material is needed for the same stress reduction.

Even though these setup is very different compared to the ones analyzed in section 3.5, the algorithm still converges within the same number of iterations and produces meaningful fiber distributions without adjusting the values of the optimization parameters.

## References

- [1] Michael Murrell, Patrick W. Oakes, Martin Lenz, and Margaret L. Gardel. Forcing cells into shape: the mechanics of actomyosin contractility. *Nature Reviews. Molecular Cell Biology*, 16(8):486–498, August 2015.
- [2] Shiladitya Banerjee, Margaret L. Gardel, and Ulrich S. Schwarz. The Actin Cytoskeleton as an Active Adaptive Material. *Annual Review of Condensed Matter Physics*, 11(1):421–439, 2020.
- [3] Pekka Lappalainen, Tommi Kotila, Antoine Jégou, and Guillaume Romet-Lemonne. Biochemical and mechanical regulation of actin dynamics. *Nature Reviews Molecular Cell Biology*, pages 1–17, August 2022. Publisher: Nature Publishing Group.
- [4] Laurent Blanchoin, Rajaa Boujemaa-Paterski, Cécile Sykes, and Julie Plastino. Actin Dynamics, Architecture, and Mechanics in Cell Motility. *Physiological Reviews*, 94(1):235–263, January 2014.
- [5] Stéphanie Pellegrin and Harry Mellor. Actin stress fibres. *Journal of Cell Science*, 120(20):3491–3499, October 2007.
- [6] Jesús M. López-Gay, Hayden Nunley, Meryl Spencer, Florencia di Pietro, Boris Guirao, Floris Bosveld, Olga Markova, Isabelle Gaugue, Stéphane Pelletier, David K. Lubensky, and Yohanns Bellaïche. Apical stress fibers enable a scaling between cell mechanical response and area in epithelial

- tissue. *Science*, 370(6514):eabb2169, October 2020. Publisher: American Association for the Advancement of Science.
- [7] Keith Burridge and Erika S. Wittchen. The tension mounts: Stress fibers as force-generating mechanotransducers. *The Journal of Cell Biology*, 200(1):9–19, July 2013.
- [8] Elena Kassianidou and Sanjay Kumar. A biomechanical perspective on stress fiber structure and function. *Biochimica et Biophysica Acta (BBA) - Molecular Cell Research*, 1853(11, Part B):3065–3074, November 2015.
- [9] Ariel Livne and Benjamin Geiger. The inner workings of stress fibers – from contractile machinery to focal adhesions and back. *J Cell Sci*, 129(7):1293–1304, April 2016.
- [10] Pirta Hotulainen and Pekka Lappalainen. Stress fibers are generated by two distinct actin assembly mechanisms in motile cells. *The Journal of Cell Biology*, 173(3):383–394, August 2006.
- [11] Sari Tojkander, Gergana Gateva, and Pekka Lappalainen. Actin stress fibers – assembly, dynamics and biological roles. *Journal of Cell Science*, 125(8):1855–1864, April 2012.
- [12] Jerome R. D. Soine, Christoph A. Brand, Jonathan Stricker, Patrick W. Oakes, Margaret L. Gardel, and Ulrich S. Schwarz. Model-based Traction Force Microscopy Reveals Differential Tension in Cellular Actin Bundles. *PLoS Comput Biol*, 11(3):e1004076, March 2015.
- [13] Ilka B. Bischofs, Franziska Klein, Dirk Lehnert, Martin Bastmeyer, and Ulrich S. Schwarz. Filamentous Network Mechanics and Active Contractility Determine Cell and Tissue Shape. *Biophysical Journal*, 95(7):3488–3496, October 2008.
- [14] Christoph A. Brand, Marco Linke, Kai Weißenbruch, Benjamin Richter, Martin Bastmeyer, and Ulrich S. Schwarz. Tension and Elasticity Contribute to Fibroblast Cell Shape in Three Dimensions. *Biophysical Journal*, 113(4):770–774, August 2017.
- [15] Jaakko I Lehtimäki, Eeva Kaisa Rajakylä, Sari Tojkander, and Pekka Lappalainen. Generation of stress fibers through myosin-driven reorganization of the actin cortex. *eLife*, 10:e60710, January 2021. Publisher: eLife Sciences Publications, Ltd.
- [16] Timothée Vignaud, Calina Copos, Christophe Leterrier, Mauricio Toro-Nahuelpan, Qingzong Tseng, Julia Mahamid, Laurent Blanchoin, Alex Mogilner, Manuel Théry, and Laetitia Kurzawa. Stress fibres are embedded in a contractile cortical network. *Nature Materials*, 20(3):410–420, March 2021. Number: 3 Publisher: Nature Publishing Group.

- [17] Sari Tojkander, Gergana Gateva, Amjad Husain, Ramaswamy Krishnan, and Pekka Lappalainen. Generation of contractile actomyosin bundles depends on mechanosensitive actin filament assembly and disassembly. *eLife*, 4:e06126, December 2015.
- [18] Adam Engler, Lucie Bacakova, Cynthia Newman, Alina Hategan, Maureen Griffin, and Dennis Discher. Substrate Compliance versus Ligand Density in Cell on Gel Responses. *Biophysical Journal*, 86(1):617–628, January 2004.
- [19] Masha Prager-Khoutorsky, Alexandra Lichtenstein, Ramaswamy Krishnan, Kavitha Rajendran, Avi Mayo, Zvi Kam, Benjamin Geiger, and Alexander D. Bershadsky. Fibroblast polarization is a matrix-rigidity-dependent process controlled by focal adhesion mechanosensing. *Nat Cell Biol*, 13(12):1457–1465, December 2011.
- [20] Shiqiong Hu, Kinjal Dasbiswas, Zhenhuan Guo, Yee-Han Tee, Visalatchi Thiagarajan, Pascal Hersen, Teng-Leong Chew, Samuel A. Safran, Ronen Zaidel-Bar, and Alexander D. Bershadsky. Long-range self-organization of cytoskeletal myosin II filament stacks. *Nature Cell Biology*, 19(2):133–141, February 2017.
- [21] Kinjal Dasbiswas, Shiqiong Hu, Frank Schnorrer, Samuel A. Safran, and Alexander D. Bershadsky. Ordering of myosin II filaments driven by mechanical forces: experiments and theory. *Phil. Trans. R. Soc. B*, 373(1747):20170114, May 2018.
- [22] Sanjay Kumar, Iva Z. Maxwell, Alexander Heisterkamp, Thomas R. Polte, Tanmay P. Lele, Matthew Salanga, Eric Mazur, and Donald E. Ingber. Viscoelastic Retraction of Single Living Stress Fibers and Its Impact on Cell Shape, Cytoskeletal Organization, and Extracellular Matrix Mechanics. *Biophysical Journal*, 90(10):3762–3773, May 2006.
- [23] Julien Colombelli, Achim Besser, Holger Kress, Emmanuel G. Reynaud, Philippe Girard, Emmanuel Caussin, Uta Haselmann, John V. Small, Ulrich S. Schwarz, and Ernst H. K. Stelzer. Mechanosensing in actin stress fibers revealed by a close correlation between force and protein localization. *Journal of Cell Science*, 122(10):1665–1679, May 2009.
- [24] Elena Kassianidou, Christoph A. Brand, Ulrich S. Schwarz, and Sanjay Kumar. Geometry and network connectivity govern the mechanics of stress fibers. *Proceedings of the National Academy of Sciences*, 114(10):2622–2627, July 2017.
- [25] Roberto Bernal, Milenka Van Hemelryck, Basile Gurchenkov, and Damien Cuvelier. Actin Stress Fibers Response and Adaptation under Stretch. *International Journal of Molecular Sciences*, 23(9):5095, January 2022. Number: 9 Publisher: Multidisciplinary Digital Publishing Institute.



- [26] Shinji Deguchi, Toshiro Ohashi, and Masaaki Sato. Tensile properties of single stress fibers isolated from cultured vascular smooth muscle cells. *Journal of Biomechanics*, 39(14):2603–2610, 2006.
- [27] Kazuo Katoh, Yumiko Kano, Michitaka Masuda, Hirofumi Onishi, and Keigi Fujiwara. Isolation and Contraction of the Stress Fiber. *Molecular Biology of the Cell*, 9(7):1919–1938, July 1998. Publisher: American Society for Cell Biology (mboc).
- [28] Achim Besser and Ulrich S Schwarz. Coupling biochemistry and mechanics in cell adhesion: a model for inhomogeneous stress fiber contraction. *New Journal of Physics*, 9:425–425, November 2007.
- [29] Matthew R. Stachowiak and Ben O’Shaughnessy. Recoil after Severing Reveals Stress Fiber Contraction Mechanisms. *Biophysical Journal*, 97(2):462–471, July 2009.
- [30] Robert J. Russell, Shen-Ling Xia, Richard B. Dickinson, and Tanmay P. Lele. Sarcomere Mechanics in Capillary Endothelial Cells. *Biophysical Journal*, 97(6):1578–1585, September 2009.
- [31] Achim Besser, Julien Colombelli, Ernst H. K. Stelzer, and Ulrich S. Schwarz. Viscoelastic response of contractile filament bundles. *Physical Review E*, 83(5):051902, May 2011.
- [32] Mariya Savinov, Charles S. Peskin, and Alex Mogilner. A model for contractile stress fibers embedded in bulk actomyosin networks, September 2024. arXiv:2409.02282 [physics].
- [33] Christian J. Cyron and Wolfgang A. Wall. Finite-element approach to Brownian dynamics of polymers. *Physical Review E*, 80(6):066704, December 2009. Publisher: American Physical Society.
- [34] Yuan Lin, X. Wei, J. Qian, K. Y. Sze, and V. B. Shenoy. A combined finite element-Langevin dynamics (FEM-LD) approach for analyzing the mechanical response of bio-polymer networks. *Journal of the Mechanics and Physics of Solids*, 62:2–18, January 2014.
- [35] Claus Heussinger and Erwin Frey. Stiff Polymers, Foams, and Fiber Networks. *Physical Review Letters*, 96(1):017802, January 2006. Publisher: American Physical Society.
- [36] Vikram S. Deshpande, Robert M. McMeeking, and Anthony G. Evans. A bio-chemo-mechanical model for cell contractility. *Proceedings of the National Academy of Sciences*, 103(38):14015–14020, September 2006.
- [37] Vikram S Deshpande, Robert M McMeeking, and Anthony G Evans. A Model for the Contractility of the Cytoskeleton Including the Effects of Stress-Fibre Formation and Dissociation. *Proceedings of the Royal Society A: Mathematical, Physical and Engineering Science*, 463(2079):787–815, August 2007.

- [38] William Ronan, Vikram S. Deshpande, Robert M. McMeeking, and J. Patrick McGarry. Cellular contractility and substrate elasticity: a numerical investigation of the actin cytoskeleton and cell adhesion. *Biomechanics and Modeling in Mechanobiology*, 13(2):417–435, June 2013.
- [39] Manuel Thery, Anne Pepin, Emilie Dressaire, Yong Chen, and Michel Bornens. Cell distribution of stress fibres in response to the geometry of the adhesive environment. *Cell Motility and the Cytoskeleton*, 63(6):341–355, June 2006.
- [40] Elena Kassianidou, Dimitri Probst, Julia Jäger, Stacey Lee, Anne-Lou Roguet, Ulrich Sebastian Schwarz, and Sanjay Kumar. Extracellular Matrix Geometry and Initial Adhesive Position Determine Stress Fiber Network Organization during Cell Spreading. *Cell Reports*, 27(6):1897–1909.e4, May 2019.
- [41] Andrea C. Scheiwe, Stephanie C. Frank, Tatjana J. Autenrieth, Martin Bastmeyer, and Martin Wegener. Subcellular stretch-induced cytoskeletal response of single fibroblasts within 3D designer scaffolds. *Biomaterials*, 44:186–194, March 2015.
- [42] Uta Faust, Nico Hampe, Wolfgang Rubner, Norbert Kirchgessner, Sam Safran, Bernd Hoffmann, and Rudolf Merkel. Cyclic Stress at mHz Frequencies Aligns Fibroblasts in Direction of Zero Strain. *PLoS ONE*, 6(12):e28963, December 2011.
- [43] Alexandra M. Greiner, Hao Chen, Joachim P. Spatz, and Ralf Kemkemer. Cyclic Tensile Strain Controls Cell Shape and Directs Actin Stress Fiber Formation and Focal Adhesion Alignment in Spreading Cells. *PLoS ONE*, 8(10):e77328, October 2013.
- [44] Ariel Livne, Eran Bouchbinder, and Benjamin Geiger. Cell reorientation under cyclic stretching. *Nature Communications*, 5(1):3938, May 2014. Bandiera\_abtest: a Cg\_type: Nature Research Journals Number: 1 Primary\_atype: Research Publisher: Nature Publishing Group Subject\_term: Biophysics;Cell biology Subject\_term\_id: biophysics;cell-biology.
- [45] Franziska Klein, Benjamin Richter, Thomas Striebel, Clemens M Franz, Georg von Freymann, Martin Wegener, and Martin Bastmeyer. Two-Component Polymer Scaffolds for Controlled Three-Dimensional Cell Culture. *Advanced Materials*, 23(11):1341–1345, March 2011.
- [46] Rabea Link, Mona Jaggy, Martin Bastmeyer, and Ulrich S. Schwarz. Modelling cell shape in 3d structured environments: A quantitative comparison with experiments. *PLOS Computational Biology*, 20(4):1–21, 04 2024.
- [47] Nathan W Goehring and Anthony A Hyman. Organelle growth control through limiting pools of cytoplasmic components. *Current Biology*, 22(9):R330–R339, 2012.

- [48] Jean Bénézech, Linus Seelinger, Peter Bastian, Richard Butler, Timothy Dodwell, Chupeng Ma, and Robert Scheichl. Scalable multiscale-spectral gfem with an application to composite aero-structures. *Journal of Computational Physics*, 508:113013, 2024.
- [49] T. Andersen, D. Wörthmüller, D. Probst, I. Wang, P. Moreau, V. Fitzpatrick, T. Boudou, U. S. Schwarz, and M. Balland. Cell size and actin architecture determine force generation in optogenetically activated cells. *Biophysical Journal*, 122(4):684–696, February 2023.
- [50] T. J. Dodwell, S. Kynaston, R. Butler, R. T. Haftka, Nam H. Kim, and R. Scheichl. Multilevel Monte Carlo simulations of composite structures with uncertain manufacturing defects. *Probabilistic Engineering Mechanics*, 63:103116, January 2021.
- [51] Peter Hansbo, Mats G. Larson, and Karl Larsson. Cut finite element methods for linear elasticity problems. In Stéphane P. A. Bordas, Erik Burman, Mats G. Larson, and Maxim A. Olshanskii, editors, *Geometrically Unfitted Finite Element Methods and Applications*, Lecture Notes in Computational Science and Engineering, pages 25–63. Springer International Publishing, 2017.
- [52] Sham Tlili, Cyprien Gay, François Graner, Philippe Marcq, François Molino, and Pierre Saramito. Colloquium: Mechanical formalisms for tissue dynamics. *The European Physical Journal E*, 38(5):33, May 2015.
- [53] Dietrich Braess. *Finite Elements: Theory, Fast Solvers, and Applications in Solid Mechanics*. Cambridge University Press, 3 edition, 2007.
- [54] Anita Hansbo and Peter Hansbo. A finite element method for the simulation of strong and weak discontinuities in solid mechanics. *Computer Methods in Applied Mechanics and Engineering*, 193(33):3523–3540, 2004.
- [55] Peter Bastian and Christian Engwer. An unfitted finite element method using discontinuous galerkin. *International Journal for Numerical Methods in Engineering*, 79(12):1557–1576, 2009.
- [56] Susanne C. Brenner, Joscha Gedicke, Li-Yeng Sung, and Yi Zhang. An a posteriori analysis of  $c^0$  interior penalty methods for the obstacle problem of clamped kirchhoff plates. *SIAM Journal on Numerical Analysis*, 55(1):87–108, 2017.
- [57] P. Bastian, M. Blatt, A. Dedner, C. Engwer, R. Klöfkorn, R. Kornhuber, M. Ohlberger, and O. Sander. A generic grid interface for parallel and adaptive scientific computing. Part II: Implementation and tests in DUNE. *Computing*, 82(2):121–138, 2008.
- [58] Peter Bastian, Markus Blatt, Andreas Dedner, Nils-Arne Dreier, Christian Engwer, René Fritze, Carsten Gräser, Christoph Grüninger, Dominic Kempf,

- Robert Klöfkorn, Mario Ohlberger, and Oliver Sander. The Dune framework: Basic concepts and recent developments. *Computers & Mathematics with Applications*, 81:75–112, 2021.
- [59] Dominic Kempf, René Heß, Steffen Müthing, and Peter Bastian. Automatic code generation for high-performance discontinuous galerkin methods on modern architectures. *ACM Trans. Math. Softw.*, 47(1), December 2020.
- [60] Timothy A. Davis. Algorithm 832: Umfpack v4.3—an unsymmetric-pattern multifrontal method. *ACM Trans. Math. Softw.*, 30(2):196–199, June 2004.
- [61] Abdullah Konak, David W. Coit, and Alice E. Smith. Multi-objective optimization using genetic algorithms: A tutorial. *Reliability Engineering & System Safety*, 91(9):992–1007, 2006.
- [62] K. Deb, A. Pratap, S. Agarwal, and T. Meyarivan. A fast and elitist multi-objective genetic algorithm: NSGA-II. *IEEE Transactions on Evolutionary Computation*, 6(2):182–197, 2002. Conference Name: IEEE Transactions on Evolutionary Computation.
- [63] Nathalie Caille, Olivier Thoumine, Yanik Tardy, and Jean-Jacques Meister. Contribution of the nucleus to the mechanical properties of endothelial cells. *Journal of Biomechanics*, 35(2):177–187, February 2002.
- [64] Sebastian Wohlrab, Sebastian Mueller, and Stephan Gekle. Mechanical complexity of living cells can be mapped onto simple homogeneous equivalents. *Biomechanics and Modeling in Mechanobiology*, 23(3):1067–1076, June 2024.
- [65] Akira Katsumi, Julie Milanini, William B. Kiosses, Miguel A. del Pozo, Roland Kaunas, Shu Chien, Klaus M. Hahn, and Martin Alexander Schwartz. Effects of cell tension on the small GTPase Rac. *The Journal of Cell Biology*, 158(1):153–164, July 2002.
- [66] Mehdi Farsad and Franck J. Vernerey. An XFEM-based numerical strategy to model mechanical interactions between biological cells and a deformable substrate. *International Journal for Numerical Methods in Engineering*, 92(3):238–267, 2012. \_eprint: <https://onlinelibrary.wiley.com/doi/pdf/10.1002/nme.4335>.
- [67] Koen Schakenraad, Jeremy Ernst, Wim Pomp, Erik H. J. Danen, Roeland M. H. Merks, Thomas Schmidt, and Luca Giomi. Mechanical interplay between cell shape and actin cytoskeleton organization. *Soft Matter*, 16(27):6328–6343, July 2020. Publisher: The Royal Society of Chemistry.
- [68] Pramod A Pullarkat, Pablo A Fernández, and Albrecht Ott. Rheological properties of the eukaryotic cell cytoskeleton. *Physics Reports*, 449(1-3):29–53, 2007.

- [69] Philip Kollmannsberger and Ben Fabry. Linear and Nonlinear Rheology of Living Cells. *Annual Review of Materials Research*, 41(1):75–97, 2011.
- [70] Chase P Broedersz and Fred C MacKintosh. Modeling semiflexible polymer networks. *Reviews of Modern Physics*, 86(3):995–1036, 2014.
- [71] Lan Lu, Sara J. Oswald, Hai Ngu, and Frank C. P. Yin. Mechanical Properties of Actin Stress Fibers in Living Cells. *Biophysical Journal*, 95(12):6060–6071, December 2008.
- [72] Michael F Staddon, Edwin M Munro, and Shiladitya Banerjee. Pulsatile contractions and pattern formation in excitable actomyosin cortex. *PLOS Computational Biology*, 18(3):e1009981, 2022.